

Key Factors for Template-Oriented Porous Titania Synthesis: Solvents and Catalysts

Shanshan Yin, Lin Song, Senlin Xia, Yajun Cheng, Nuri Hohn, Wei Chen, Kun Wang, Wei Cao, Shujin Hou, and Peter Müller-Buschbaum*

Various types of titania nanostructures are synthesized with a polymer-templated sol-gel method based on the amphiphilic diblock copolymer polystyrene-*b*-polyethylene oxide (PS-*b*-PEO) in combination with selective incorporation of the titania precursor titanium tetraisopropoxide. Custom tailoring of different types of titania morphologies is realized by changing the phase separation behavior of the PS-*b*-PEO template. Particularly, application of solvents from different categories is found to have a major impact upon the phase separation behavior of PS-*b*-PEO and the final titania film morphology. The amount of available hydrochloric acid catalyst during the gelation process is seen as an additional key factor to induce controllable morphological changes. Scanning electron microscopy and grazing incidence small angle X-ray scattering measurements are carried out to study the surface and inner structure of porous titania films. Systematic analysis and comparison of different characterization results allow attributing the following three factors to the respectively formed titania nanostructure: the surface energy between PS blocks and surrounding solvent, the aggregation behavior of the titania nanoparticles, and the block-specific selectivity of the used solvent. For all synthesized titania thin films, an anatase-type crystallization is confirmed through X-ray powder diffraction.


is in particular interesting, when used as the anode material of lithium/sodium ion batteries, because titania with a high surface-to-volume ratio facilitates penetration of electrolyte and intercalation of lithium or sodium ions.^[12–15] In the case of organic-inorganic hybrid solar cells, the exciton diffusion length within typical backfilling materials is typically less than 20 nm. Mesoporous titania with uniform pore arrangement provides an excellent basis to suppress recombination losses of excitons.^[11,16–18] Although many achievements have been reached in the preparation of porous metal oxide materials, current synthetic methods still have several inherent drawbacks from the perspective of thin film nanotechnology, such as time consuming processing conditions and the ill-defined powder form product.^[19–23] Among plenty of preparation routes to porous inorganic nanostructures, amphiphilic block copolymer assisted sol-gel chemistry features a low-cost, operation

1. Introduction

During the past decades, nanostructured titania thin films have been widely studied due to their attractive properties such as high electron mobility and mechanical flexibility.^[1–6] In particular mesoporous titania films were successfully used in energy related applications. Examples include various types of next-generation solar cells, gas sensing, lithium/sodium ion batteries, and photocatalysis.^[7–11] Mesoporous titania in thin films

compatibility with ambient atmosphere and easy one-pot processing route, and therefore has been confirmed as a particularly promising approach.^[24–29] In this block copolymer assisted synthetic route, the hydrolysis and condensation products of the organic precursors are preferentially incorporated into one of the blocks through hydrogen bonds. Accordingly, the morphology control of the corresponding functional inorganic part can be realized by phase separation behavior of the sol-gel solution.^[30–35] Templin and coauthors prepared a kind of organically modified

S. Yin, Dr. L. Song, Dr. S. Xia, Dr. N. Hohn, W. Chen, Dr. K. Wang, W. Cao, Prof. P. Müller-Buschbaum
Physik-Department
Lehrstuhl für Funktionelle Materialien
Technische Universität München
James-Franck-Str. 1, 85748 Garching, Germany
E-mail: muellerb@ph.tum.de

 The ORCID identification number(s) for the author(s) of this article can be found under <https://doi.org/10.1002/smt.201900689>.

© 2020 The Authors. Published by WILEY-VCH Verlag GmbH & Co. KGaA, Weinheim. This is an open access article under the terms of the Creative Commons Attribution License, which permits use, distribution and reproduction in any medium, provided the original work is properly cited.

DOI: 10.1002/smt.201900689

Dr. L. Song
Institute of Flexible Electronics
Northwestern Polytechnical University
127 West Youyi Road, 710072 Xi'an, Shanxi, P. R. China
Prof. Y. Cheng
Ningbo Institute of Materials Technology and Engineering
Chinese Academy of Sciences
1219 Zhongguan West Road, 315201 Ningbo, Zhejiang, P. R. China
S. Hou
Physik-Department
Physics of Energy Conversion and Storage
Technische Universität München
James-Franck-Straße 1, 85748 Garching, Germany
Prof. P. Müller-Buschbaum
Heinz Maier-Leibnitz Zentrum (MLZ)
Technische Universität München
Lichtenbergstr. 1, D-85748 Garching, Germany

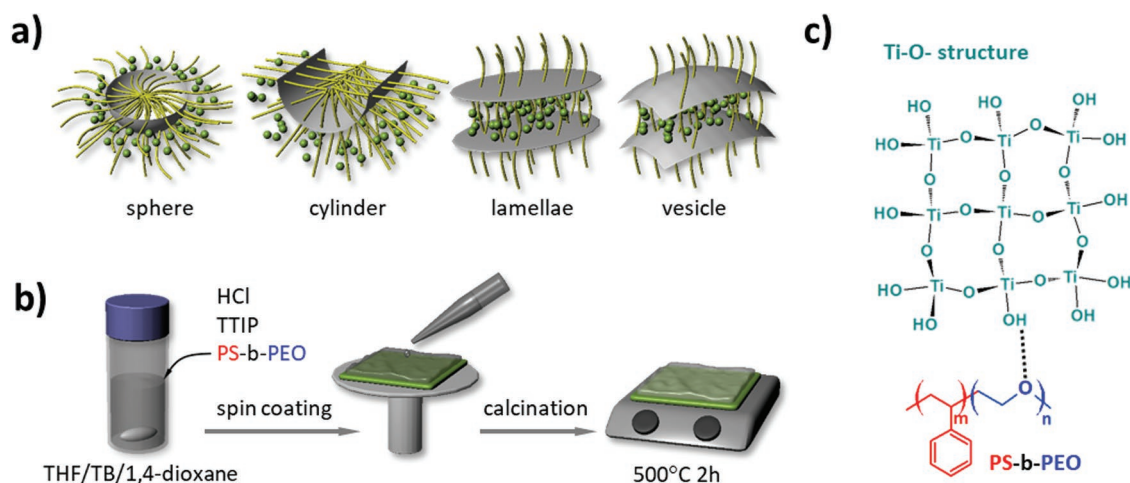


Figure 1. a) Illustration of different polymer template (yellow chains)/titania nanoparticles (green) arrangements formed in the sol-gel solution. b) Schematic overview of the preparation process of porous titania thin films. Casting solutions are based on different solvents and HCl content as indicated in the insets. Subsequent spin coating and high temperature annealing leads to the formation of porous and crystalline titania thin films. c) Representation of the linkage between titania species and the PEO block through hydrogen bonding.

aluminosilicate mesostructures from amphiphilic poly(isoprene-*b*-ethylene oxide) block copolymers. Various morphologies corresponding to the phase diagrams of diblock copolymers were obtained by increasing the fraction of the inorganic precursors with respect to the polymer.^[36] The Smarsly's group constructed a kind of highly crystalline mesoporous SnO₂ film by evaporation-induced self-assembly using a novel amphiphilic block-copolymer template.^[37] Fisher and coauthors obtained a series of nanopatterned titania thin films by organic/inorganic self-assembly and selective local functionalization.^[38] Cheng et al. successfully synthesized nanowires, nanoparticles, flake-like structures, nanodoughnuts, and worm-like and foam-like nanoscale networks by controlling the relative content of precursor, catalyst, and solvent in a polystyrene-*b*-polyethylene oxide (PS-*b*-PEO) based casting solution.^[39] Similarly, Hohn et al. demonstrated the strong influence of hydrochloric acid (HCl) addition on the resulting thin film morphology.^[16] Solvent effects on surfactant templated mesoporous sol-gel silica systems were, e.g., studied by Kruk and co-workers.^[40,41] However, to the best of our knowledge, a similar study about the block copolymer assisted sol-gel titania synthesis has been rarely studied, which is also of great importance to the final thin morphologies.^[42-44] In the microphase-separated sol-gel system, the swelling degree of the polymer chains in each domain is significantly influenced by the solvent nature. Typically, a neutral solvent is equally distributed into each domain, therefore swells both blocks to the same extent. Otherwise, a preferential swelling for a certain domain will be induced even with a slight solvent selectivity.^[45,46] In the present work, the morphology evolution of the template-oriented titania nanostructures has been systematically studied in terms of different solvents category and HCl content. Specifically, tetrahydrofuran (THF), azeotrope of toluene and 1-butanol (TB), and 1,4-dioxane are used for the stock sol-gel solution preparation, respectively. Five parallel samples with exponentially increased HCl content are prepared in each kind of solvent. After sufficient stirring, titania incorporated micellar solution is spin coated onto silicon substrates for thin film deposition. After removing the polymer template by calcination, various intriguing titania scaffolds are obtained. Different types of micelle structures, such as sphere, cylinder,

lamellae, and vesicle, formed in the stock solution are schematically exhibited in **Figure 1a**. Hydrolyzed titania nanoparticles are depicted as green and polymer chains are represented as yellow, respectively. **Figure 1b** illustrates the thin film synthetic route utilized in the present work and **Figure 1c** shows the hydrogen interaction between Ti-O- structures and PEO blocks. The real space imaging method scanning electron microscopy (SEM) and the reciprocal space method grazing-incidence small angle X-ray scattering (GISAXS) are used for the thin film morphology characterization. Based on the detailed comparison and analysis of the multiscale characterization results, the relationship between the sol-gel components and final thin film morphology is unveiled.

2. Result and Discussion

The self-assembly behavior of amphiphilic block polymers can be provoked by two approaches, progressive addition of poor solvent or solvent evaporation. For a poor solvent induced self-assembly, the micellization of polymer chains occurs when the poor solvent content increases to a critical value. This critical point is related to the concentration and molecular weight of the block polymer.^[47] For the solvent evaporation induced self-assembly process, the microphase-separated structures can be formed at a critical polymer concentration. This micellization critical point varies with the Flory-Huggins interaction parameter and polymerization degree of the block polymer.^[48,49] During the self-assembly process in aqueous solutions, the energetically unfavorable water-hydrophobe interactions are avoided for preventing a large enthalpy penalty. However, the degree of freedom of single chains is decreased significantly ($\Delta S < 0$). Consequently, the phase separation is induced by the increased free energy in the system ($\Delta G > 0$)^[50,51]

$$\Delta G = \Delta H - T\Delta S \quad (1)$$

Figure 2 refers to the SEM images of the titania thin films prepared with THF as a solvent. As shown in the ternary phase diagram of the stock solution (**Figure 2f**), the HCl content increases from 0.5 vol% to 1.0 vol%, 2.0 vol%, 4.0 vol%, and 8.0 vol% for

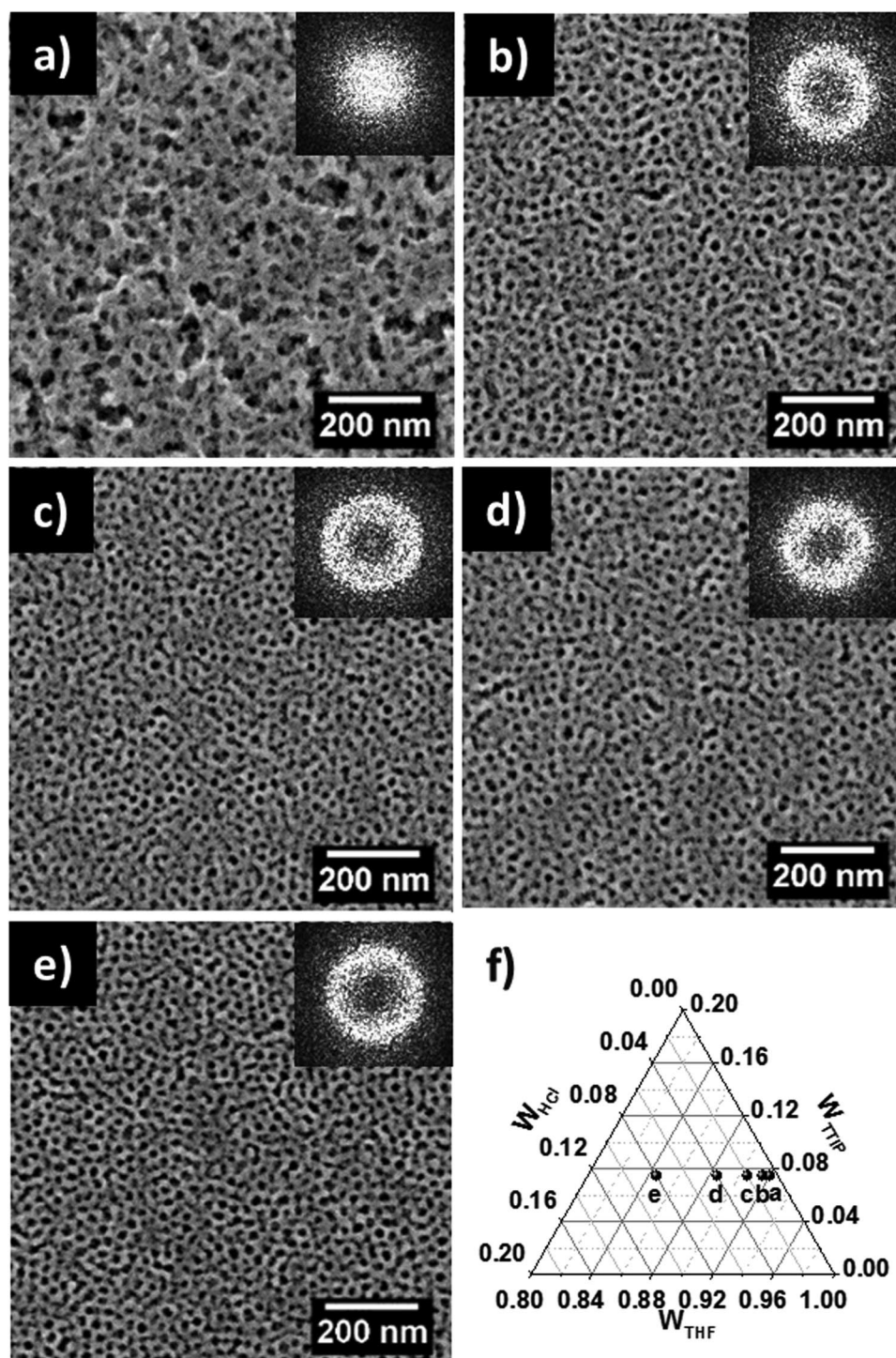


Figure 2. SEM images of the titania thin films prepared with THF solvent. The upper right insets refer to the corresponding fast Fourier transform (FFT) patterns. The volume fraction of HCl is exponentially increased from a) 0.5 vol% to e) 8.0 vol%. f) Component phase diagram of the respective samples.

sample shown in Figure 2a–e. The volume fraction of titanium tetraisopropoxide (TTIP) in each sample is kept constant at 7.5 vol%. It can be seen that all SEM images in Figure 2 exhibit an interconnected, porous titania phase.^[39] When the HCl content in the stock solution is increased from 0.5 vol% to 1.0 vol%, a significant enhancement of ordering can be observed (Figure 2a,b). The

porous structure appears to be stable after the HCl content exceeds 2 vol% (Figure 2c–e). The structural evolution from Figure 2a–e is also reflected in the fast Fourier transform (FFT) patterns of the corresponding SEM images. The rather well defined ring-like pattern in Figure 2–e indicates the presence of pores with similar size and enhanced ordering, while the smeared out pattern in

Figure 2a indicates a rather broad size distribution with more disorder. The underlying mechanism governing the thin film structure evolution can be analyzed with the following two approaches. The first approach is based on the chemical properties of the components in the sol-gel solution, considering the superior miscibility of TTIP and PS-*b*-PEO in the solvent THF and the chemical stability of each component. The phase separation behavior is supposed to be less affected by these chemicals. However, TTIP is quite easily hydrolyzed by H₂O molecules. The hydrolysis reaction mechanism between TTIP and H₂O molecules belongs to a S_N2 nucleophilic substitution, which is schematically shown in Figure S1 (Supporting Information). Considering the catalyst role of H₂O molecules in the HCl solution, the lowest 0.5 vol% HCl addition in the present work is assumed to be enough to stimulate the hydrolysis reaction (Figure S1I and S1II, Supporting Information). However, regarding the condensation process, a further growth and agglomeration process of the condensed titania nanoparticles is prone to occur with a low HCl addition. Since the isoelectric point of TiO₂ lies at a pH of 5–7, charges on the particle surfaces in a weak acidic medium are not sufficient for keeping discrete particles in a dispersed state, which facilitates the formation of randomly arranged large pore structures.^[16,42] A second approach is based on the phase separation behavior of the diblock copolymer in the sol-gel solution. As mentioned before, the phase separation of a diblock copolymer can be provoked by solvent evaporation or poor solvent addition. The similar synthetic process in our previous work demonstrated the randomly arranged titania nanostructures formed without HCl addition,^[16] which suggested the weak effect of the solvent-induced self-assembly for the final titania nanostructures. Accordingly, the structure evolution in Figure 2 can also be assigned to the surface energy variation between PS blocks and surrounding solvent associated with poor solvent addition. For the titania structure in Figure 2a, 0.5 vol% HCl addition within the sol-gel solution is lower than the critical value for micellization. As a result, a weak phase-separated mixture of titania nanoparticles, polymer chains, and solvent is formed in the solution, which is converted into a rather random structure after spin coating and calcination process.^[52,53] With the increase of HCl addition, a distinct phase-separated structure is observed in Figure 2b, which suggests the critical poor solvent content is located between 0.5 vol% and 1.0 vol%. Closer observation shows that all phase-separated structures in Figure 2b–e are nearly isoporous, meaning that they exhibit a narrow pore size distribution as can be identified by the sharp peaks of the power spectral density (PSD) profiles in Figure S5 (Supporting Information). The formation of spherical micelles at higher poor solvent content can be assigned to the enhanced surface energy between PS blocks and poor solvent. The stretch of hydrophobic PS blocks can be significantly inhibited with micellization. In addition, with higher HCl volume fraction, the aggregation process of hydrolyzed titania nanoparticles is effectively suppressed by an enhanced electrostatic repulsion force, which makes it easier to follow the microphase-separated structure of polymer template. Interestingly, quite similar titania thin film morphologies are exhibited if the HCl content increases from 1.0 vol% to 8.0 vol%, which indicates the superior stability of the phase-separated system under different poor solvent contents.

The SEM topography shows the nanostructure evolution of the titania thin films for a local surface region. Besides

the local morphology, the thin film homogeneity over a large region is an important requirement for practical applications. GISAXS is a powerful tool to detect the surface and buried structures in the thin film.^[54] Because of the very small incident angle, a macroscopic footprint of X-ray allows for gaining structure information with a high statistical relevance.^[55]

Figure 3a–e refers to the 2D GISAXS data of the titania thin films prepared with different HCl content in THF solvent. The observable maximum scattering intensity between the specular peak and sample horizon is the so-called Yoneda peak, which is material characteristic.^[18] The very pronounced horizontal scattering signal at the Yoneda region indicates the statistical average information of the titania nanostructures in the lateral direction. The shape of the scattering patterns from Figure 3a–e clearly demonstrates the variance of the structure within the film. Compared with Figure 3a, the appearance of the pronounced vertical Bragg rods in Figure 3b–e indicates the ordered pore arrangement within the probed thin film.^[32]

For quantitative analysis, the horizontal line cuts at the Yoneda peak position are performed (the position is indicated by the red arrow in Figure 3a). As shown in Figure 3f, the broad shoulder in line cut of the thin film prepared with 0.5 vol% HCl could be attributed to the nanostructures with a relatively disordered spatial arrangement. In contrast, the well-defined Bragg peaks appeared with an increased HCl content imply a narrow size distribution and ordered spatial arrangement of the nanostructures. The structure features obtained from the GISAXS data are in good agreement with the observation from the SEM measurements (Figure 2). Moreover, the feature size variation could be manifested by a closer observation of the peak positions (vertical black dash lines in Figure 3f). The first-order peak of the thin film prepared with 2.0 vol%, 4.0 vol%, and 8.0 vol% HCl is found at the same position, which is slightly right shifted with respect to the 1.0 vol% HCl addition. The relatively lower q_y value for the thin film with 1.0 vol% HCl indicates the presence of larger structure distances.

In addition, when the HCl addition increases from 1.0 vol% to 8.0 vol%, the peak position of the two lattice peaks in the GISAXS profiles remains in the same ratio of $1:\sqrt{3}$, which indicates the existence of hexagonally packed structures inside the films, whereas SEM does not show such order on the film surface.^[45] The average spacing d of the microphase-separated structures can be determined from the first-order Bragg diffraction peak q_m by using $d = 2\frac{\pi}{q_m}$. The calculated average spacing d of the thin films with HCl content of 1.0 vol%, 2.0 vol%, 4.0 vol%, and 8.0 vol% is 30, 26, 26, and 26 nm, respectively.

In order to extract quantitative structure information along the lateral direction, horizontal line cuts are fitted within the framework of the Distorted-Wave Born Approximation (DWBA) using an effective interface approximation and local monodisperse approximation. Gaussian-distributed form factors in the applied model represent scattering centers placed on a 1D paracrystal lattice with a characteristic center-to-center distance.^[56] The scattering signal is approximated by incoherently superposing the scattering intensities of the individual standing cylinder substructures, which are parameterized with a radius (Figure S2, Supporting Information).^[57] Error bars indicate the scope of

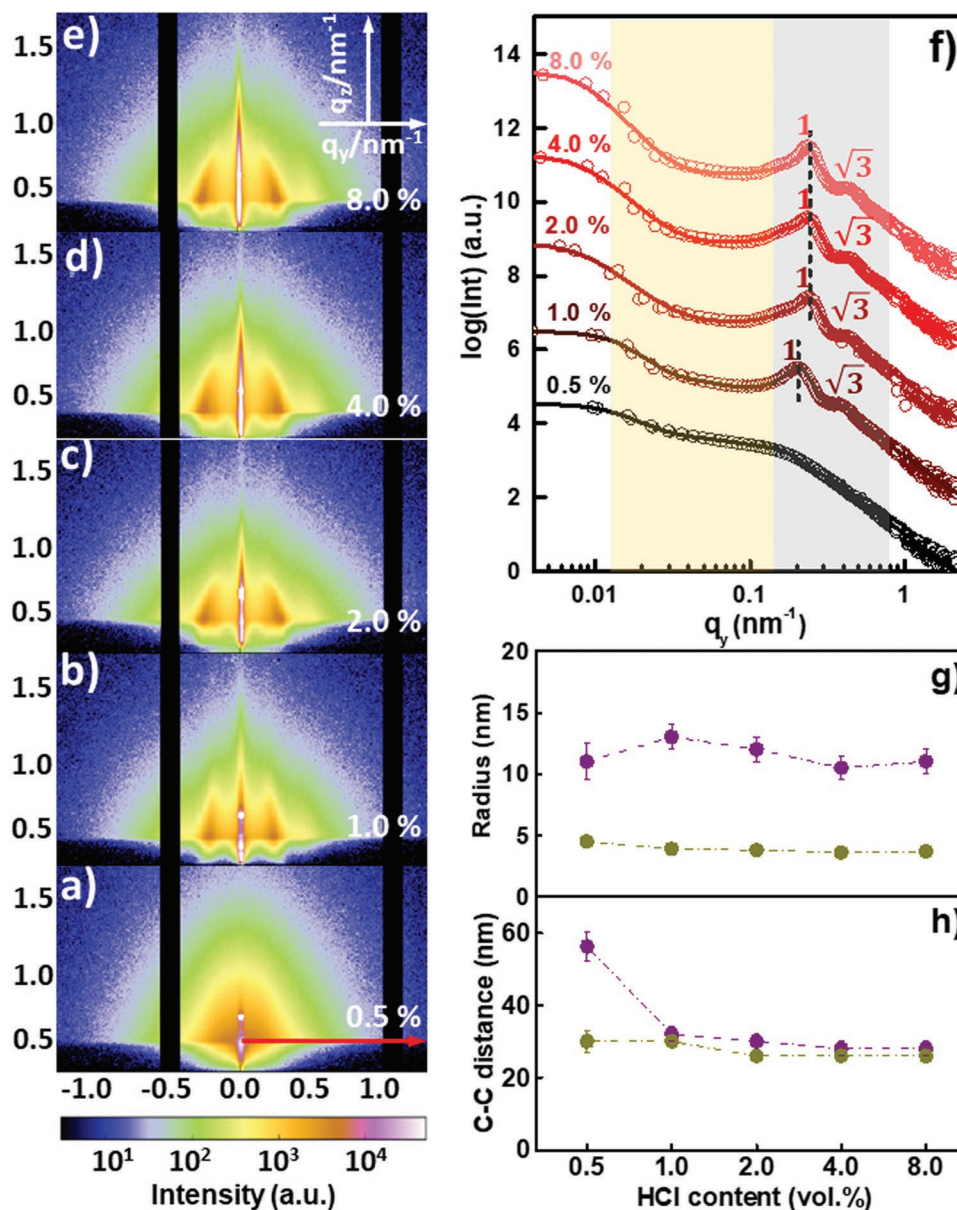


Figure 3. a–e) 2D GISAXS data of the titania thin films prepared with THF solvent, the corresponding HCl content added in the sol–gel solution is noted in the lower right corner and the position for the horizontal line cut is shown with a red arrow; f) horizontal line cuts of the 2D GISAXS data. The measured data are plotted as hollow circles and the fitting results are shown as solid lines, respectively. All curves are shifted along the intensity axis for clarity of presentation. Extracted structure g) radii and h) center-to-center distances as a function of the HCl content. Dark yellow circles refer to the small-sized structure and purple circles indicate the large-sized structure.

goodness of fit. Within this model, all data in Figure 3f are fitted with two structure factors (center-to-center distances) and two form factors (radii). As marked by the gray area in Figure 3f, the pronounced scattering peaks in high q region are well fitted with small radii and center-to-center distances, which are indicated by the dark yellow circles in Figure 3g,h. Specifically, the center-to-center distance of the thin films with 0.5 vol%, 1.0 vol%, 2.0 vol%, 4.0 vol%, and 8.0 vol% HCl is fitted to be (30 ± 3) nm, (30 ± 1) nm, (26 ± 1) nm, (26 ± 1) nm, and (26 ± 1) nm, which are well consistent with the preliminary calculation result by using $d = 2\frac{\pi}{q_m}$.^[45] The corresponding structure radii are fitted to be (4.5 ± 0.3) nm, (3.9 ± 0.5) nm, (3.8 ± 0.3) nm, (3.6 ± 0.4) nm,

and (3.7 ± 0.4) nm. Therefore, the average pore sizes of the titania thin films can be extracted by the following equation^[17]

$$\text{Pore size} = \text{center to center distance} - 2 \times \text{structure radius} \quad (2)$$

The pore sizes of the thin films with 0.5 vol%, 1.0 vol%, 2.0 vol%, 4.0 vol%, and 8.0 vol% HCl are determined to be (21 ± 4) nm, (22 ± 2) nm, (18 ± 2) nm, (19 ± 2) nm, and (19 ± 2) nm, respectively, which are in good agreement with the SEM topography shown in Figure 2.

The features in the low q_y region, marked with the yellow part in Figure 3f, indicate the existence of large structures. The

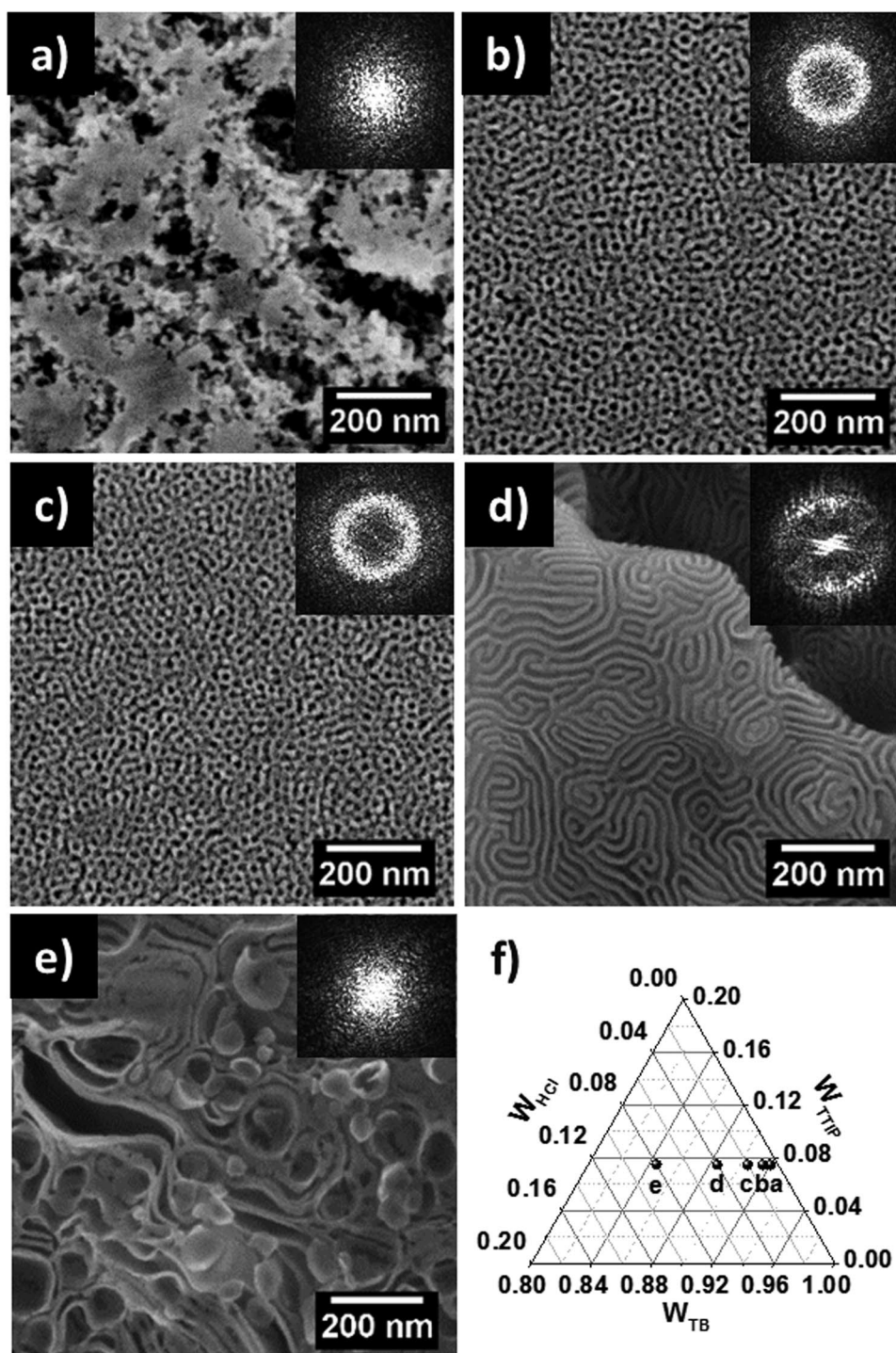


Figure 4. SEM images of the titania thin films prepared with TB azeotrope solvent. The upper right insets refer to the corresponding fast Fourier transform (FFT) patterns. The volume fraction of HCl is exponentially increased from a) 0.5 vol% to e) 8.0 vol%. f) Component phase diagram of the respective samples.

fitted center-to-center distances and radii are represented as purple circles as shown in Figure 3g,h, respectively. Specifically, the center-to-center distances of the thin films prepared with 0.5 vol%, 1.0 vol%, 2.0 vol%, 4.0 vol%, and 8.0 vol% HCl are (56 ± 4) nm, (32 ± 2) nm, (30 ± 2) nm, (28 ± 2) nm, and (28 ± 2) nm. The corresponding radii are (11 ± 2) nm, (13 ± 1) nm,

(12 ± 1) nm, (10 ± 1) nm, and (11 ± 1) nm. With the same method mentioned above, the pore size calculated for the large structures for the samples with 0.5 vol%, 1.0 vol%, 2.0 vol%, 4.0 vol%, and 8.0 vol% HCl is (34 ± 7) nm, (4 ± 2) nm, (6 ± 4) nm, (7 ± 4) nm, and (6 ± 4) nm. These are also visible within the SEM images. The good consistency of the SEM topography and

the GISAXS data suggests that the surface morphology is also present within the bulk of the thin films.

Figure 4 refers to the titania nanostructures prepared with different HCl addition to the TB solvent. As shown in Figure 4a,b, when the volume fraction of HCl increases from 0.5 vol% to 2.0 vol%, a significant structural transition from large clusters to nearly isoporous nanostructures is visible, which can also be reflected by the corresponding FFT patterns and PSD profiles in Figure S5 (Supporting Information).

When the volume fraction of HCl reaches 4.0 vol%, the sol-gel solution turns out to be turbid, which may result from the formation of micrometer-sized aggregates in the solution.^[39] Because of the existence of these aggregates, the spin-coated thin films with 4.0 vol% HCl exhibit discontinuous structures, which is well visible under low magnification in the SEM topography (Figure S2a). Figure 4d shows the uneven lamellar structure within a large aggregate. A further HCl addition yields a coexistence of lamellae and vesicle structures (Figure 4e). The structure transition mechanism with progressive HCl addition in Figure 4 can also be illustrated from the perspective of the chemical properties of the components and surface energy in the solution. Similar to the random structure formed in the THF system, the structure formed with 0.5 vol% HCl in Figure 4a could also be attributed to the synergistic effect of the weak repulsion force among the hydrolyzed titania nanoparticles and inferior phase separation tendency of the block polymer. With the increase of the HCl content, the well-dispersed titania nanoparticles in combination with the enhanced phase separation tendency of the diblock polymer facilitate the templating effect in the sol-gel solution. As mentioned before, the final morphology of titania thin films is almost unaffected by the solvent-induced self-assembly process. Thus, it is reasonable to ascribe the thin film morphology to the phase separation condition of the casting solution. It is noteworthy that, with progressive poor solvent addition in the block co-polymer solution, the spherical micelles are usually the first aggregates to form and they can be considered as the starting morphology for other aggregates, because the PS chains in spherical micelles are usually more stretched than in cylinders, lamellae, or vesicles.^[50] With the increased surface energy between PS blocks and poor solvent, the stretching of the PS chains is greatly reduced. As a consequence, a more thermodynamically favorable morphology, such as lamellae and vesicles, is formed. The coexistence structure of lamellae and vesicle in Figure 4e could be explained by the following three scenarios. First, the stability boundaries for lamellae and vesicle are overlapping during the poor solvent addition process.^[58] Second, the coexistence of lamellae and vesicle might be a true thermodynamic phenomenon, which depends on the free energy difference between them.^[59] Third, the polydispersity of the bulk polymer may also account for the coexistence of the structures.^[60]

Compared with the morphologies shown in Figure 2, more intriguing structures, such as cylinder, lamellae and vesicle structures in Figure 4d,e, are obtained in the TB sol-gel system. Considering the low dielectric constant of the solvent (THF: 7.58; TB: 6.79; and 1,4-dioxane: 2.25) and nonionizing properties of the PS and PEO blocks, the repulsion force among the polymer chains provoked by ionization is negligible.^[50] Therefore the morphology variation of the titania thin film with

Table 1. Characteristics of the different solvent and polymer.

	δ [MPa ^{1/2}]				V_s [cm ³ /mol]
	δ_d	δ_p	δ_h	δ_H	
THF	19.4	16.8	5.7	8.0	79.7
TB ^{a)}	19.6	17.4	2.6	5.9	101.8
1,4-dioxane	20.5	19.0	1.8	7.4	88.5
PS	18.6	18.6	0.2	0.0	–
PEO	19.9	17.3	3.0	9.4	–

^{a)}The azeotrope solvent of toluene and 1-butanol.

Note: R is 8.3144598 J mol⁻¹ K⁻¹ and T is 298 K.

respect to different solvent category can be analyzed in the perspective of the polymer-solvent interaction parameter (χ)^[61]

$$\chi_{P-S} = V_s (\delta_s - \delta_p)^2 / RT + 0.34 \quad (3)$$

where V_s and δ_s are the molar volume and solubility parameter of the solvent, δ_p is the solubility parameter of the polymer, R is the gas constant, and T is the temperature. The characteristics of the different solvents and polymers can be taken from the literature (e.g., polymer handbook; Table 1).^[62] As shown in Table 1, the solubility parameter of the solvent (Hansen solubility parameter δ_H) consists of three parts: dispersive δ_d , permanent dipole-dipole interaction δ_p , and hydrogen bonding forces δ_h

$$\delta_H^2 = \delta_d^2 + \delta_p^2 + \delta_h^2 \quad (4)$$

In the case of the mixed TB solvent, the solubility parameter and molar volume are calculated by the sum of the products of the component values with their volume fractions.^[63] The volume ratio of toluene and 1-butanol in the mixed solvent is 71.4:28.6 in this work. Table 2 refers to the corresponding polymer-solvent interaction parameters calculated by Equation (3). According to Flory-Huggins theory, the polymer and solvent are completely miscible when χ_{P-S} is less than 0.5, and the smaller χ_{P-S} value means the better solubility of the polymer. As shown in Table 2, all of the solvents used in this work are good solvents for both PS and PEO blocks. Nevertheless, the difference between χ_{S-PS} and χ_{S-PEO} gives the preferential affinity of the solvent for a certain block (Equation (4))

$$\Delta\chi = \chi_{S-PS} - \chi_{S-PEO} \quad (5)$$

According to Table 2 and Equation (5), the $\Delta\chi$ of THF and TB is 0.01 and 0.04, respectively, which suggests both of the solvents have a slightly preferential affinity for the PEO block.

Table 2. Polymer-solvent interaction parameters (χ_{P-S}) of different polymer-solvent pairs.

χ_{P-S}	THF	TB ^{a)}	1,4-dioxane
PS	0.36	0.38	0.47
PEO	0.35	0.34	0.35

^{a)}The azeotrope solvent of toluene and 1-butanol.

In addition, compared with THF, the relative higher $\Delta\chi$ of TB implies the stronger affinity between the PEO block and the TB solvent, which means the higher swelling degree of the PEO domain in the TB solvent. The different preferential affinity of THF and TB solvent for the polymer blocks might be the reason for the different morphologies seen in Figures 2 and 4. The morphological difference is only conspicuous at 4.0 vol% and 8.0 vol% HCl content, and very similar morphologies are shown with 0.5 vol% and 2.0 vol% HCl addition. Thus, it is concluded that when two kinds of solvent possess comparable $\Delta\chi$ value, the spin coated thin films prefer to show similar micro-phase-separated structures under relative low HCl content.

While a distinct morphology deviation will be manifested with progressive HCl addition.

The 2D GISAXS data of the titania thin films prepared with TB solvent are shown in Figure 5a–e. Regarding the thin films prepared with 0.5 vol% and 8.0 vol% HCl, the smeared scattering patterns in the lateral direction can be assigned to the wide size distribution of the nanostructures oriented parallel to the silicon substrate (corresponding to the SEM images of Figure 4a,e). In comparison, two symmetrically arranged Bragg peaks are shown for the thin film prepared with 1.0 vol% and 2.0 vol% HCl addition, which signifies a highly organized arrangement in the lateral direction. Compared with 2D

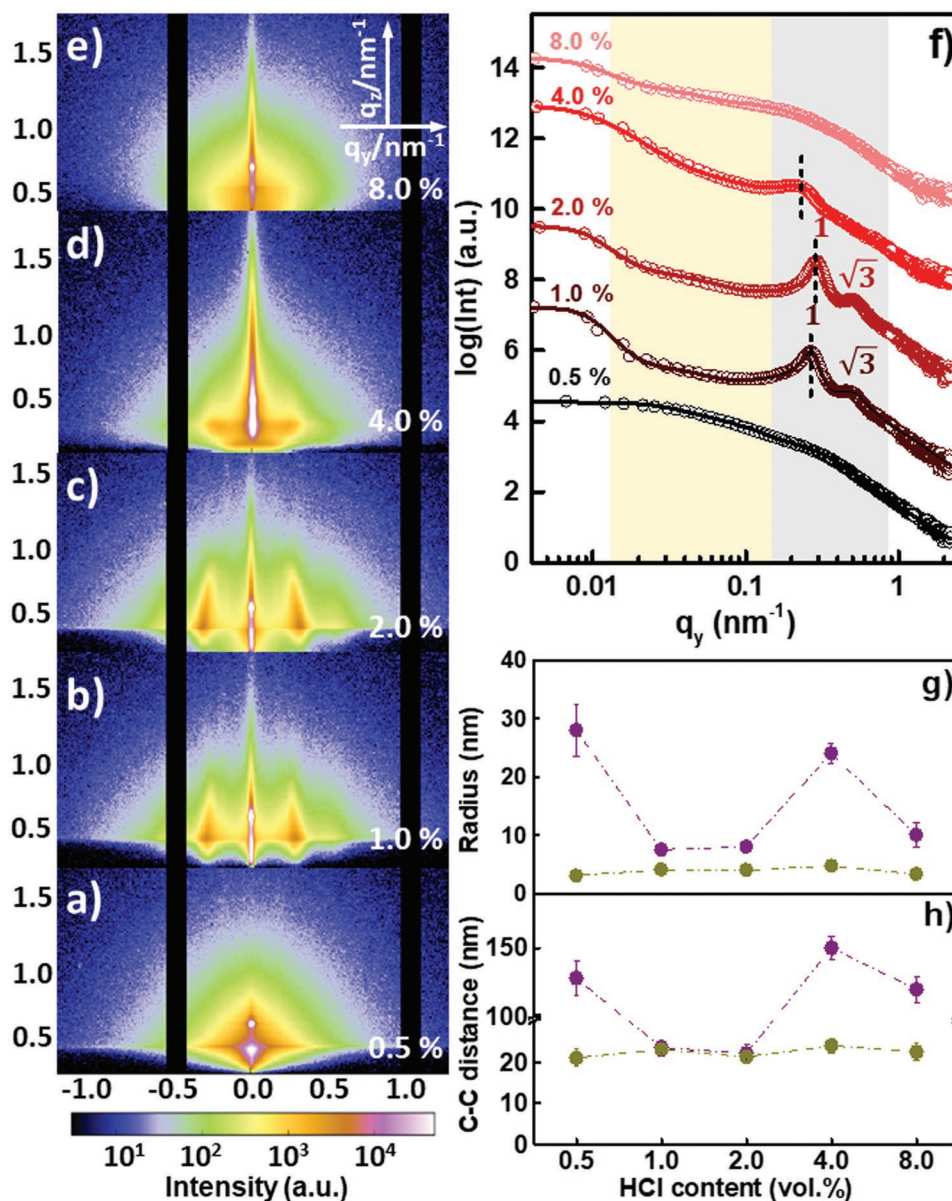


Figure 5. a–e) 2D GISAXS data of the titania thin films prepared with TB azeotrope solvent; the corresponding HCl content added in the sol–gel solution is noted in the lower right corner; f) horizontal line cuts of the 2D GISAXS data. The measured data are plotted as hollow circles and the fitting results are shown as solid lines, respectively. All curves are shifted along the intensity axis for clarity of presentation. Extracted structure g) radii and h) center-to-center distances as a function of the HCl content. Dark yellow circles refer to the small-sized structure and purple circles indicate the large-sized structure.

GISAXS data in Figure 5b,c, a greatly broadened scattering peak in the case of 4.0 vol% HCl addition is observed in Figure 5d, which might result from the anisotropic structure of the cylinders (Figure 4d).

Moreover, compared with other 2D GISAXS data, two intensity maxima are visible between the specular beam and sample horizon in Figure 5d. As mentioned before, because of the formation of large aggregates, the thin film prepared with 4.0 vol% HCl addition exhibits discontinuous structures on the silicon substrate. Figure S3 (Supporting Information) demonstrates the significant structural difference between the aggregates and the region marked with the red frame. It is known that the scattering signal in the vertical direction is associated with the material density, and the sporadic titania species scattered on the silicon wafer possess a much lower density than that of the aggregates. Thus, it is reasonable to ascribe the additional peak at lower scattering angle to these low-density titania structures. To determine whether the scattering signal comes from the silicon substrate or the titania layer, an additional GISAXS characterization of the bare silicon substrate is performed under the same incident angle. According to the 2D GISAXS data of bare silicon in Figure S3b (Supporting Information), a weak Yoneda peak is visible between the specular beam and sample horizon only. To further compare the Yoneda peak position of silicon and titania thin films, the vertical line cuts at the same q_y value are performed and shown in Figure S3d (Supporting Information). It is observed that the silicon substrate and the titania thin film possess quite close Yoneda region at around 0.2° , and the additional peak at low q_y position for titania is not found in the vertical line cut of the silicon substrate. Therefore, the particular peak for titania at the low q_y region can be assigned to the discontinuous titania nanostructures on the silicon substrate.

For a quantitative analysis, the horizontal line cuts at the Yoneda region of porous titania are performed and shown in Figure 5f. The horizontal line cuts in low q_y and high q_y region can be analyzed separately as a function of the shape and intensity difference of the scattering peaks. Regarding the high q_y region in the gray area, the significantly smeared peak seen in the horizontal line cuts of the thin films prepared with 0.5 vol% and 8.0 vol% HCl is caused by the wide size distribution of the nanostructures. On the other hand, for the thin films prepared with 1.0 vol%, 2.0 vol%, and 4.0 vol% HCl, pronounced scattering peaks are observed. The first-order peaks of the three line cuts are marked with black dash lines, which can be used to roughly estimate the spacing d of the microphase-separated structures by the equation of $d = 2\frac{\pi}{q_m}$. The calculated d value for the thin film prepared with 1.0 vol%, 2.0 vol% HCl is 24 nm, 22 nm, which can be assigned to the spacing between the neighboring nanowalls (Figure 4b,c). As mentioned before, the surface energy between the PS block and the surrounding solvent increases with continuous HCl addition. As a result, the stretch of the hydrophobic PS chains is progressively inhibited, which leads to the decrease of the pore size from 24 nm (Figure 4b) to 22 nm (Figure 4c). Furthermore, the relative positions of the first and second-order Bragg peaks of the samples prepared with 1.0 vol% and 2.0 vol% HCl are also following a $1:\sqrt{3}$ ratio, which again suggests the presence of hexagonally organized structures over a macroscopic scale. The d value of

the thin film prepared with 4.0 vol% HCl is calculated to be 28 nm, which can be attributed to the distance between the adjacent cylinders (Figure 4d).

Similarly, in the framework of the DWBA, all line cuts in Figure 5f are well fitted with two structure factors and two form factors. The large structures are denoted as purple circles and small structures are represented as dark yellow circles, respectively (Figure 5g,h). The pronounced scattering signals in high q_y region are well fitted with small structures. Specifically, the center-to-center distance of the thin films prepared with 0.5 vol%, 1.0 vol%, 2.0 vol%, 4.0 vol%, and 8.0 vol% HCl is fitted to be (21 ± 2) nm, (23 ± 1) nm, (21 ± 1) nm, (24 ± 2) nm, and (22 ± 2) nm. The corresponding radii are (3.0 ± 0.3) nm, (4.1 ± 0.2) nm, (4.0 ± 0.1) nm, (4.7 ± 0.5) nm, and (3.3 ± 0.5) nm. With the method mentioned above, the calculated pore size contributed by the small structures is (15 ± 3) nm, (15 ± 2) nm, (13 ± 1) nm, (15 ± 3) nm, and (16 ± 3) nm. On the other hand, the scattering signals at low q_y region are fitted with large structures. The center-to-center distance of the large structures with 0.5 vol%, 1.0 vol%, 2.0 vol%, 4.0 vol%, and 8.0 vol% HCl addition is fitted to be (128 ± 13) nm, (25 ± 2) nm, (22 ± 2) nm, (150 ± 10) nm, and (120 ± 10) nm. The corresponding radii are (28.0 ± 4.5) nm, (7.5 ± 0.4) nm, (8.0 ± 0.2) nm, (24.0 ± 1.8) nm, and (10.0 ± 2.1) nm. As a result, the pore size afforded by the large structures is (72 ± 2) nm, (9 ± 3) nm, (6 ± 3) nm, (102 ± 12) nm, and (100 ± 14) nm. The much higher pore radii within the thin films prepared with 0.5 vol%, 4.0 vol%, and 8.0 vol% HCl can be clearly observed in Figure S4 (Supporting Information).

Figure 6 refers to the SEM images of titania thin film prepared with 1,4-dioxane. As shown in Figure 6a,b and similar with the THF and TB system, the randomly stacked nanostructures are obtained with low HCl addition (0.5 vol% and 1.0 vol%), which can be assigned to the weak phase separation conditions of the sol-gel solution and aggregation of the nanoparticles. However, with increasing HCl addition, such as in the case of the volume fraction of 2.0 vol% in Figure 6c, a coexisting structure of nanowires and large aggregates is obtained. The formation of these inhomogeneous structures could be attributed to the variation of the surface energy between PS blocks and surrounding solvent. Compared with the random structures, the formation of the nanowires in Figure 6c effectively accommodates the extra surface energy resulting from the higher HCl content. However, the decreased surface energy associated with the phase transition makes it difficult to maintain the stability of the new sol-gel system. As a result, some large aggregates are formed. With a further HCl addition, the aggregation process is significantly inhibited by the enhanced surface energy between the PS blocks and the surrounding solvent. Consequently, the structures with high specific surface area are formed as seen in Figure 6d,e. As mentioned before, for the microphase-separated block polymer system, the spherical micelles are usually the first aggregates to form. However, unlike the thin film prepared with THF and TB, the structure transition from random to sphere is not found in the case of 1,4-dioxane. The direct structure transition from a random to a cylinder morphology might be attributed to the formation of large aggregates in the case of 1.0 vol% HCl addition. These aggregates possess much larger size than that of

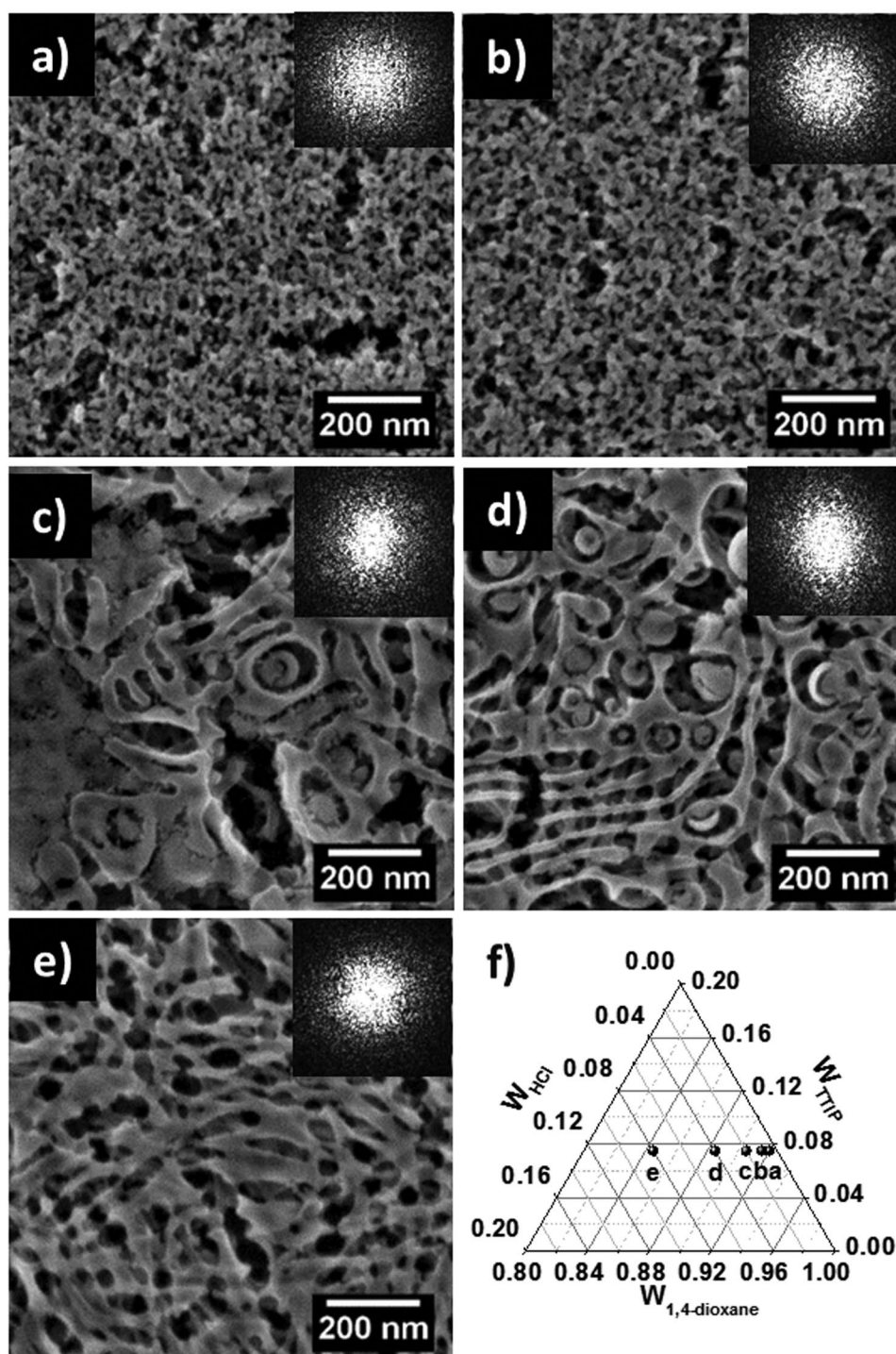


Figure 6. SEM images of the titania thin films prepared with 1,4-dioxane solvent. The upper right insets refer to the corresponding fast Fourier transform (FFT) patterns. The volume fraction of HCl is exponentially increased from a) 0.5 vol% to e) 8.0 vol%. f) Component phase diagram of the respective samples.

the microphase-separated cylinders, which consumes plenty of TTIP. As a result, the TTIP or Ti–O– content in the microphase-separated regions is significantly decreased. Since the stretch of the PEO blocks region can be modified by the content of hydrophilic Ti–O– structures, a new microphase-separated morphology might be provoked by the formation of the

aggregates. In addition, compared with THF and TB, the much higher $\Delta\chi$ value of 1,4-dioxane cause a full stretching of the PEO block, which also facilitates the formation of more asymmetric microphase-separated structures.

The 2D GISAXS data and corresponding horizontal line cuts are shown in Figure 7a–f. It is observed that for all samples a

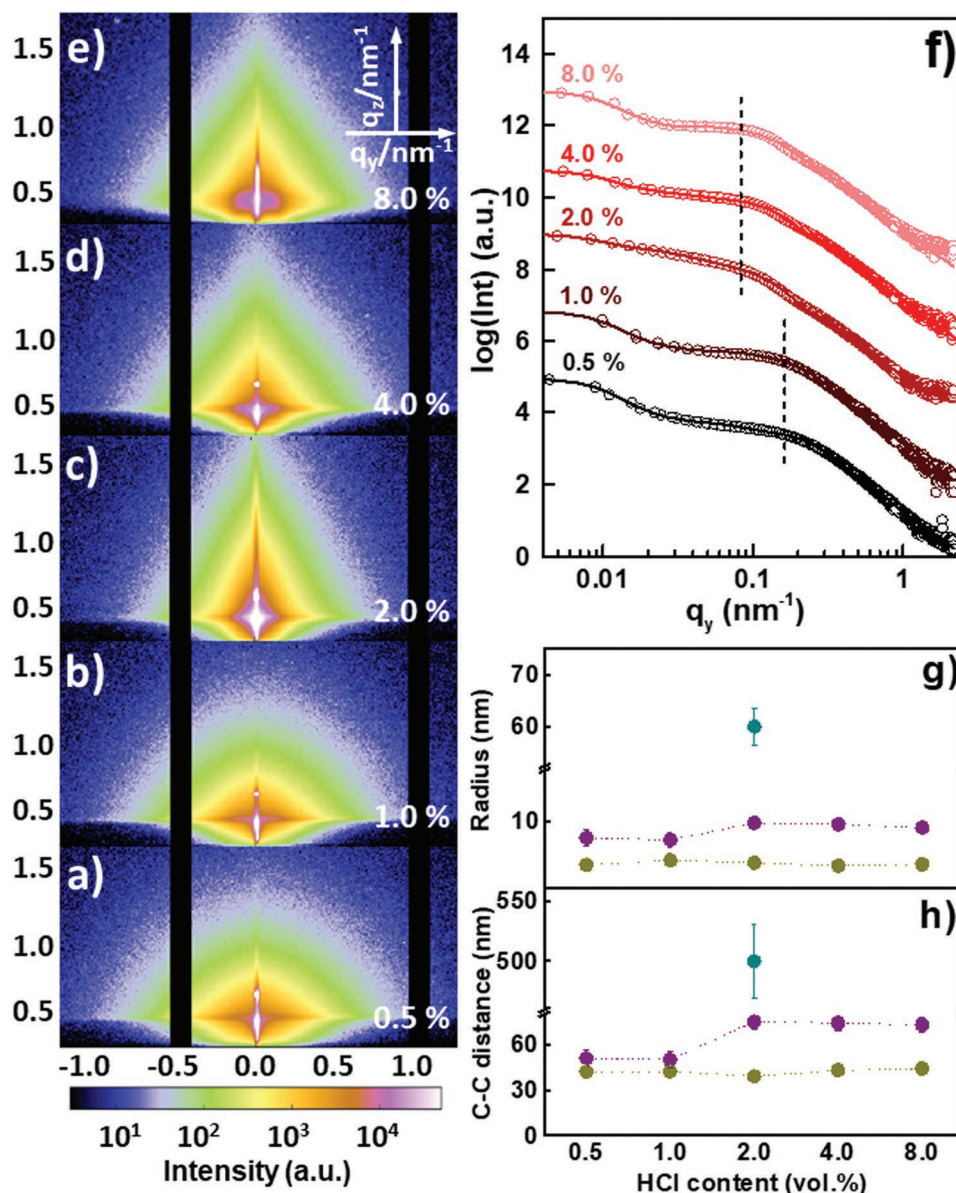


Figure 7. a–e) 2D GISAXS data of the titania thin films prepared with 1,4-dioxane solvent; the corresponding HCl content added in the sol-gel solution is noted in the lower right corner; f) horizontal line cuts of the 2D GISAXS data. The measured data are plotted as hollow circles and the fitting results are shown as solid lines, respectively. All curves are shifted along the intensity axis for clarity of presentation. Extracted structure g) radii and h) center-to-center distances as a function of the HCl content. The fitted small, middle and large structures are represented as dark yellow, purple, and dark cyan colors, respectively.

smear peak along the q_y -axis is present, which signifies the wide size distribution and random orientation of the structures within the thin film.^[57] However, a peak center can still be found for each horizontal line cut, which is marked with a black dashed line in Figure 7f. The shift of the broad peaks with progressive HCl addition suggests the increase of the pore size within the thin films.

Similarly, for a quantitative analysis, all horizontal line cuts at the Yoneda position are fitted in the framework of the DWBA. As shown in Figure 7g,h, the thin films prepared with 0.5 vol%, 1.0 vol%, 4.0 vol%, and 8.0 vol% HCl are fitted with two structure factors and two form factors. The large structures are denoted as purple circles and small structures are represented

as dark yellow circles, respectively (Figure 7g,h). For the small structures, the center-to-center distance of the thin films with 0.5 vol%, 1.0 vol%, 2.0 vol%, 4.0 vol%, and 8.0 vol% HCl addition is fitted to be (42 ± 4) nm, (42 ± 3) nm, (43 ± 4) nm, and (44 ± 5) nm. The corresponding radii are (3.5 ± 0.9) nm, (4.2 ± 1.0) nm, (3.4 ± 1.0) nm, and (3.6 ± 1.0) nm. As a result, the pore size contributed by the small structures is (35 ± 5) nm, (34 ± 5) nm, (36 ± 6) nm, and (37 ± 7) nm. For the large structures, the center-to-center distance of the thin films prepared with 0.5 vol%, 1.0 vol%, 4.0 vol%, and 8.0 vol% HCl is fitted to be (51 ± 5) nm, (50 ± 5) nm, (74 ± 5) nm, and (73 ± 5) nm. The corresponding radii are (7.5 ± 1.2) nm, (7.2 ± 1.1) nm,

(9.5 ± 1.0) nm, and (9.0 ± 1.0) nm. With the method mentioned above, the calculated pore size contributed by the large structures is (36 ± 7) nm, (36 ± 7) nm, (55 ± 7) nm, and (55 ± 7) nm. However, for the thin film prepared with 4.0 vol% HCl addition, an additional large structure factor and form factor in terms of the aggregates are introduced for getting a good fitting result. As shown in Figure 7g,h, the fitted small, middle, and large structures are represented as dark yellow, purple, and dark cyan colors, respectively. The center-to-center distance of the small, middle, and large structures is fitted to be (39 ± 4) nm, (75 ± 5) nm, and (500 ± 30) nm. The corresponding structures radii are (3.8 ± 1.0) nm, (9.7 ± 1.0) nm, and (60 ± 5) nm. Therefore, the calculated pore size contributed by the small, middle, and large structures is (31 ± 6) nm, (56 ± 7) nm, and (380 ± 37) nm, respectively.

In order to comprehensively compare the nanostructures synthesized with different solvent category and HCl content, the combined surface and cross-section SEM images of all titania thin films are listed in Figure S4 (Supporting Information). According to Figure S4 (Supporting Information), the high structural consistency at the surface and cross-section suggests the isotropic characteristics of the nanostructures within the bulk of the thin films. Furthermore, it is found that the peak positions and broadness shown in the PSD profiles exhibit good consistency with the horizontal line cuts of the GISAXS data, which suggests the superior homogeneity of the thin films over a large area (Figure S5, Supporting Information). Based on the SEM topography shown in Figure S4 (Supporting Information), a schematic phase diagram of PS-*b*-PEO/titania composite as a function of HCl content and $\Delta\chi$ value is plotted and shown in Figure 8a. It is observed that, when the HCl volume fraction is 0.5 vol%, all of the thin films exhibit random structures, which can be assigned to the low surface energy between the PS blocks and the surrounding solvent. With the progressive addition of HCl, different phase-separated nanostructures are formed. In THF solvent, no obvious structure variation can be observed from 1.0 vol% to 8.0 vol% HCl addition, which suggests the weak influence of HCl content on thin film morphology under low $\Delta\chi$ value. However, a significant structure variation occurs at the region of $\Delta\chi > 0.01$ and $W_{\text{HCl}} > 0.5$ vol%. At this region, a structure transition from sphere to cylinder, and then to lamellae-vesicle mixture is observed in the case of TB solvent. For 1,4-dioxane, a structure transition from random to cylinder-aggregates mixture and then to cylinder is exhibited. The different structures formed with the same HCl content can be assigned to the different $\Delta\chi$ values of the solvent, which determines the different preferential affinity of the solvent to a certain block.

It is reported that the crystallinity of titania can be modified by changing the pH value of the sol-gel solvent.^[64] Therefore, X-ray diffraction (XRD) measurements are performed for all thin films with a 2θ range from 15° to 50°. As shown in Figure 8b, the diffraction peaks at 25.3°, 36.9°, 37.9°, 38.6°, and 48.1° can be assigned to the (101), (103), (004), (112), and (200) crystal planes of anatase titania phase (JCPDS No. 02-0387). It is observed that the diffraction peaks of all thin films are found in the same position, which suggests no variation in crystallinity is provoked by HCl addition in the present work. Moreover, for the thin film prepared with 8.0 vol% HCl addition in TB solvent, the integrally enhanced peak intensity might simply be caused by more

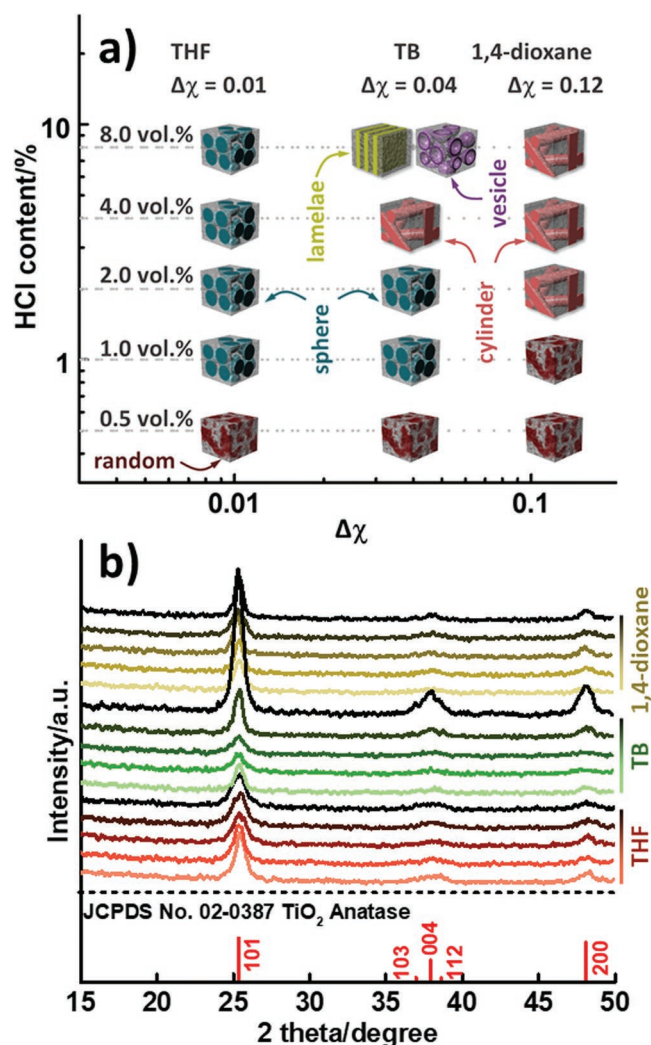


Figure 8. a) Phase diagram of PS-*b*-PEO/titania composite prepared with different solvent and HCl content, and b) X-ray diffraction (XRD) patterns of the calcined thin films. The HCl concentration from 0.5 vol% to 8.0 vol% in the stock solution is represented with gradient colors (the 8.0 vol% HCl content is denoted as black color).

material contributing to the scattering. The titania grain sizes for all samples are calculated by using the Scherrer's equation

$$D = \frac{0.9\lambda}{\beta \cos \theta} \quad (6)$$

where λ refers to the wavelength of the X-rays. β denotes the full-width at half maximum in radians, and θ is the Bragg angle. The calculated grain sizes are listed in Table 3. The different grain size of titania can be explained from the perspective of the thin film morphology and the HCl content in the sol-gel solution. Regarding the thin films prepared with THF, it is observed that the grain size of titania is inversely related to the HCl content in the sol-gel solution. The smaller grain size of titania prepared with higher HCl content can be assigned to the enhanced electrostatic interactions among the particle surfaces. In contrast in the THF system, the larger grain size formed at relative higher

Table 3. The calculated grains size of different TiO₂ thin films.

Solvent	Grain size of titania prepared with different HCl content/nanometer				
	0.5 vol%	1.0 vol%	2.0 vol%	4.0 vol%	8.0 vol%
THF	9.8	7.8	7.4	7.2	7.1
TB ^{a)}	13.1	7.5	7.5	12.9	11.1
1,4-dioxane	10.5	10.2	13.8	12.9	11.3

^{a)}The azeotrope solvent of toluene and 1-butanol.

HCl content in the TB and 1,4-dioxane system can be assigned to the formation of a new morphology. For instance, the large grain size of titania formed with 4.0 vol% and 8.0 vol% HCl addition in the TB system can be attributed to the formation of cylinder and vesicle structures. Similarly, the big crystal size obtained with 2.0 vol%, 4.0 vol%, and 8.0 vol% HCl addition in the 1,4-dioxane system can be ascribed to the formation of novel cylinder structures.

3. Conclusion

The synthesis of amphiphilic block co-polymer templated titania nanostructures is systematically investigated in terms of solvent category and HCl content. For the pore structure characterization, real space SEM measurements and reciprocal space GISAXS measurements are performed. The detailed comparison and analysis demonstrate that the structural transformation for titania thin films in terms of different HCl addition and solvent category is governed by a synergistic effect of the following three factors: first, the surface energy between PS blocks and surrounding solvent; second, the aggregation behavior of the titania nanoparticles; and third, the preferential affinity of solvent. As a poor solvent and catalyst for TTIP hydrolysis, the HCl content affects the degree of stretching of the hydrophilic PS blocks and the aggregation process of the titania nanoparticles. The solvent selectivity determines the swelling degree of both blocks. Higher solvent selectivity signifies a more asymmetrical solvent distribution within the microphase-separated domains, and higher HCl addition results in a more severe contraction of the PS blocks. When the volume fraction of HCl is 0.5 vol%, a random structure is preferred to form regardless of the solvent selectivity, which can be assigned to the unsuppressed aggregation of titania nanoparticles and weak phase separation within the thin films. With low solvent selectivity and proper HCl addition, such as in the case of the thin films prepared with THF and 1.0 vol%, 2.0 vol%, 4.0 vol%, and 8.0 vol% HCl addition, the almost equally distributed solvent within two phases and proper surface energy account for the formation of iso-porous structures. Regarding the medium solvent selectivity of TB, a typical transition from sphere, cylinder, lamellae, to vesicle related to the variation of surface energy is provoked with the HCl addition. In the case of the high solvent selectivity of 1,4-dioxane, more asymmetric nanostructures, such as cylinder, are formed by the high preferential affinity of the solvent for the PEO blocks. Irrespective of the morphology, all titania thin films consist of a pure anatase phase, which offers tremendous potential in the

applications such as gas sensor or as energy materials for photocatalysis and photovoltaics.

4. Experimental Section

Materials: Polystyrene-*b*-poly (ethylene oxide) (PS₂₀₅₀₀-*b*-PEO₈₀₀₀) was obtained from Polymer Source Inc. TTIP (97%), tetrahydrofuran (99.9%), 1,4-dioxane (99.8%), toluene (99.8%), 1-butanol (≥99%), and concentrated HCl (37%) were purchased from Sigma-Aldrich and used without further treatment.

Sol-Gel Stock Solution Preparation: For the preparation of the stock solution with THF as the solvent, PS-*b*-PEO (42.6 mg) was first dissolved in THF (1.5 mL) under continuous stirring for 1 h. Then a certain amount of TTIP was added into the mixture drop wise. In order to avoid the formation of big clusters in the sol-gel solution, the catalyst (37% HCl) was diluted with THF (0.5 mL) before adding it into the as-prepared mixture solution of PS-*b*-PEO and TTIP. The final volume fraction of TTIP in all stock solution was kept at 7.5 vol% for each sample, while the corresponding HCl content exponentially increased from 0.5 vol% to 8.0 vol%. The exact same preparation routine was carried out with 1,4-dioxane or TB (toluene and 1-butanol) instead of THF to probe the impact of different solvent categories.

Thin Film Preparation: The mixed stock solution was stirred for 1 h to stabilize the hydrogen bond formed between PEO and Ti-O species. Afterward, titania thin film deposition was performed with a Delta 6 RC TT spin coater (SÜSS Micro Tec Lithography GmbH) at 2000 rpm for 60 s. In order to remove the polymer template, the as spun thin films were calcined at 500 °C for 2 h with a heating rate of 5 °C min⁻¹ under ambient atmosphere.

Thin Film Characterization: The surface morphology of porous titania thin films was characterized by high-resolution field emission SEM (Zeiss Gemini NVision 40) at a working distance of 3.9 mm and an acceleration voltage of 5 kV. GISAXS measurements were carried out in house with a Ganesha SAXSLAB instrument at Technical University of Munich.

The following parameters were used: a wavelength of 1.54 Å, a sample to detector distance of 1056.2 mm, a horizontal beam size of 200 μm, and a vertical beam size of 100 μm. A Pilatus 300K detector (Dectris Ltd.) was used for acquisition of scattering data. An incident angle of 0.4° was set to probe inner structures of the thin film. XRD measurements were performed with X'Pert PRO PANalytical instrument (Bragg-Brentano geometry with fixed divergence slits, continuous mode, position sensitive detector, Cu-Kα radiation, Ni filter).

Supporting Information

Supporting Information is available from the Wiley Online Library or from the author.

Acknowledgements

This work was supported by funding from the Deutsche Forschungsgemeinschaft (DFG, German Research Foundation) under Germany's Excellence Strategy—EXC 2089/1—390776260 (e-conversion), TUM.solar in the context of the Bavarian Collaborative Research Project Solar Technologies Go Hybrid (SolTech), the Center for NanoScience (CeNS), and the International Research Training Group 2022 Alberta/ Technical University of Munich International Graduate School for Environmentally Responsible Functional Hybrid Materials (ATUMS). S.Y., L.S., S.X., W.C., K.W., and W.C. acknowledge the China Scholarship Council (CSC). The authors thank Prof. Alexander Holleitner and Peter Weiser for providing access to the SEM. In addition, the authors gratefully acknowledge Simon J. Schaper, Nian Li., Julian E. Heger, and Xinyu Jiang for their precious comments on the manuscript.

Conflict of Interest

The authors declare no conflict of interest.

Keywords

GISAXS, morphology, nanostructures, sol-gel synthesis, titania

Received: October 7, 2019

Revised: November 11, 2019

Published online: January 15, 2020

- [1] I. Dundar, M. Krichevskaya, A. Katerski, I. O. Acik, *R. Soc. Open Sci.* **2019**, *6*, 181578.
- [2] A. Hagfeldt, G. Boschloo, L. Sun, L. Kloo, H. Pettersson, *Chem. Rev.* **2010**, *110*, 6595.
- [3] J. L. Vivero-Escoto, Y. D. Chiang, K. Wu, Y. Yamauchi, *Sci. Technol. Adv. Mater.* **2012**, *13*, 013003.
- [4] Y. T. Liao, C. W. Huang, C. H. Liao, J. C. S. Wu, K. C. W. Wu, *Appl. Energy* **2012**, *100*, 75.
- [5] J. E. Chen, H. Y. Lian, S. Dutta, S. M. Alshehri, Y. Yamauchi, M. T. Nguyen, T. Yonezawa, K. C. Wu, *Phys. Chem. Chem. Phys.* **2015**, *17*, 27653.
- [6] H. W. Chen, C. Y. Hong, C. W. Kung, C. Y. Mou, K. C. W. Wu, K. C. Ho, *J. Power Sources* **2015**, *288*, 221.
- [7] R. Terzian, N. Serpone, C. Minero, E. Pelizzetti, *J. Catal.* **1991**, *128*, 352.
- [8] C. Chu, J. Yang, Q. Zhang, N. Wang, F. Niu, X. Xu, J. Yang, W. Fan, Y. Qian, *ACS Appl. Mater. Interfaces* **2017**, *9*, 43648.
- [9] L. Birkefeld, M. Aazd, S. Akbar, *J. Am. Ceram. Soc.* **1992**, *75*, 2964.
- [10] X. Wang, J. Q. Meng, M. Wang, Y. Xiao, R. Liu, Y. Xia, Y. Yao, E. Metwalli, Q. Zhang, B. Qiu, Z. Liu, J. Pan, L. D. Sun, C. H. Yan, P. Müller-Buschbaum, Y. J. Cheng, *ACS Appl. Mater. Interfaces* **2015**, *7*, 24247.
- [11] N. Hohn, S. J. Schlosser, L. Bießmann, S. Grott, S. Xia, K. Wang, M. Schwartzkopf, S. V. Roth, P. Müller-Buschbaum, *Nanoscale* **2018**, *10*, 5325.
- [12] Y. Ren, L. J. Hardwick, P. G. Bruce, *Angew. Chem. Int. Ed.* **2010**, *49*, 2570.
- [13] J. Lee, Y. S. Jung, S. C. Warren, M. Kamperman, S. M. Oh, F. J. DiSalvo, U. Wiesner, *Macromol. Chem. Phys.* **2011**, *212*, 383.
- [14] S. M. Oh, J. Y. Hwang, C. S. Yoon, J. Lu, K. Amine, I. Belharouak, *ACS Appl. Mater. Interfaces* **2014**, *6*, 11295.
- [15] D. Fattakhova-Rohlfing, M. Wark, T. Brezesinski, B. M. Smarsly, J. Rathouský, *Adv. Funct. Mater.* **2007**, *17*, 123.
- [16] N. Hohn, S. J. Schlosser, L. Bießmann, L. Song, S. Grott, S. Xia, K. Wang, M. Schwartzkopf, S. V. Roth, P. Müller-Buschbaum, *ACS Appl. Nano Mater.* **2018**, *1*, 4227.
- [17] L. Song, W. Wang, V. Körstgens, D. Moseguí González, F. C. Löhner, C. J. Schaffer, J. Schlipf, K. Peters, T. Bein, D. Fattakhova-Rohlfing, S. V. Roth, P. Müller-Buschbaum, *Nano Energy* **2017**, *40*, 317.
- [18] L. Song, W. Wang, V. Körstgens, D. M. González, Y. Yao, N. K. Minar, J. M. Feckl, K. Peters, T. Bein, D. Fattakhova-Rohlfing, G. Santoro, S. V. Roth, P. Müller-Buschbaum, *Adv. Funct. Mater.* **2016**, *26*, 1498.
- [19] C. J. Brinker, Y. F. Lu, A. Sellinger, H. Fan, *Adv. Mater.* **1999**, *11*, 579.
- [20] C. Sanchez, C. Boissière, D. Grosso, C. Laberty, L. Nicole, *Chem. Mater.* **2008**, *20*, 682.
- [21] J. Lee, M. C. Orillall, S. C. Warren, M. Kamperman, F. J. DiSalvo, U. Wiesner, *Nat. Mater.* **2008**, *7*, 222.
- [22] S. W. Robbins, P. A. Beaucage, H. Sai, K. W. Tan, J. K. Werner, J. P. Sethna, F. J. DiSalvo, S. M. Gruner, R. V. Dover, U. Wiesner, *Sci. Adv.* **2016**, *2*, e1501119.
- [23] T. Weller, L. Deilmann, J. Timm, T. S. Dorr, P. A. Beaucage, A. S. Cherevan, U. B. Wiesner, D. Eder, R. Marschall, *Nanoscale* **2018**, *10*, 3225.
- [24] G. Kaune, M. Memesa, R. Meier, M. A. Ruderer, A. Diethert, S. V. Roth, M. D'Acunzi, J. S. Gutmann, P. Müller-Buschbaum, *ACS Appl. Mater. Interfaces* **2009**, *1*, 2862.
- [25] T. S. Dörr, S. Fleischmann, M. Zeiger, I. Grobelsek, P. W. de Oliveira, V. Presser, *Chem. - Eur. J.* **2018**, *24*, 6358.
- [26] J. Chen, Z. Hua, Y. Yan, A. A. Zakhidov, R. H. Baughman, L. Xu, *Chem. Commun.* **2010**, *46*, 1872.
- [27] L. Kavan, J. Rathouský, M. Gratzel, V. Shklover, A. Zukal, *J. Phys. Chem. B* **2000**, *104*, 12012.
- [28] M. G. Fischer, X. Hua, B. D. Wilts, I. Gunkel, T. M. Bennett, U. Steiner, *ACS Appl. Mater. Interfaces* **2017**, *9*, 22388.
- [29] M. Rawolle, M. A. Niedermeier, G. Kaune, J. Perlich, P. Lellig, M. Memesa, Y. J. Cheng, J. S. Gutmann, P. Müller-Buschbaum, *Chem. Soc. Rev.* **2012**, *41*, 5131.
- [30] J. H. Pan, X. S. Zhao, W. I. Lee, *Chem. Eng. J.* **2011**, *170*, 363.
- [31] Y. Xiao, S. You, Y. Yao, T. Zheng, C. Lin, S. V. Roth, P. Müller-Buschbaum, W. Steffen, L. D. Sun, C. H. Yan, J. S. Gutmann, M. Yin, J. Fu, Y. J. Cheng, *Eur. J. Inorg. Chem.* **2013**, *8*, 1251.
- [32] Y. J. Cheng, S. Zhou, M. Wolkenhauer, G. G. Bumbu, S. Lenz, M. Memesa, S. Nett, S. Emmerling, W. Steffen, S. V. Roth, J. S. Gutmann, *Eur. J. Inorg. Chem.* **2014**, *5*, 836.
- [33] K. Nakanishi, *Mater. Res. Soc.* **2007**, *1007*, S01.
- [34] M. C. Fuentes, G. J. Soler-Illia, *Chem. Mater.* **2006**, *18*, 2109.
- [35] Y. Cheng, L. J. Zhi, W. Steffen, J. S. Gutmann, *Chem. Mater.* **2008**, *20*, 6580.
- [36] M. Templin, A. Franck, A. D. Chesne, H. Leist, Y. Zhang, R. Ulrich, V. Schädler, U. Wiesner, *Science* **1997**, *278*, 1795.
- [37] T. Brezesinski, A. Fischer, K. I. Iimura, C. Sanchez, D. Grosso, M. Antonietti, B. M. Smarsly, *Adv. Funct. Mater.* **2006**, *16*, 1433.
- [38] A. Fischer, M. Kuemmel, M. Järn, M. Linden, C. Boissière, L. Nicole, C. Sanchez, D. Grosso, *Small* **2006**, *2*, 569.
- [39] Y. J. Cheng, J. S. Gutmann, *J. Am. Chem. Soc.* **2006**, *128*, 4658.
- [40] L. Huang, M. Kruk, *Chem. Mater.* **2015**, *27*, 679.
- [41] L. Cao, T. Man, M. Kruk, *Chem. Mater.* **2009**, *21*, 1144.
- [42] C. C. Wang, J. Y. Ying, *Chem. Mater.* **1999**, *11*, 3113.
- [43] C. J. Brett, N. Mittal, W. Ohm, M. Gensch, L. P. Kreuzer, V. Körstgens, M. Månsson, H. Frielinghaus, P. Müller-Buschbaum, L. D. Söderberg, S. V. Roth, *Macromolecules* **2019**, *52*, 4721.
- [44] S. C. Warren, L. C. Messina, L. S. Slaughter, M. Kamperman, Q. Zhou, S. M. Gruner, F. J. DiSalvo, U. Wiesner, *Science* **2008**, *320*, 1748.
- [45] B. Nandan, M. K. Vyas, M. Böhme, M. Stamm, *Macromolecules* **2010**, *43*, 2463.
- [46] S. Kataoka, Y. Takeuchi, A. Kawai, M. Yamada, Y. Kamimura, A. Endo, *Langmuir* **2013**, *29*, 13562.
- [47] L. F. Zhang, H. W. Shen, A. Eisenberg, *Macromolecules* **1997**, *30*, 1001.
- [48] T. Ghoshal, A. Chaudhari, C. Cummins, M. T. Shaw, J. D. Holmes, M. A. Morris, *Soft Matter* **2016**, *12*, 5429.
- [49] Y. Funaki, K. Kumano, T. Nakao, H. Jinnai, H. Yoshida, K. Kimishima, K. Tsutsumi, Y. Hirokawa, T. Hashimoto, *Polymer* **1999**, *40*, 7147.
- [50] Y. Mai, A. Eisenberg, *Chem. Soc. Rev.* **2012**, *41*, 5969.
- [51] J. Hwang, C. Jo, K. Hur, J. Lim, S. Kim, J. Lee, *J. Am. Chem. Soc.* **2014**, *136*, 16066.
- [52] G. H. Fredrickson, *Macromolecules* **1989**, *22*, 1238.
- [53] E. Helfand, Y. Tagami, *J. Chem. Phys.* **1972**, *56*, 3592.
- [54] P. Müller-Buschbaum, M. Garcia-Gutierrez, A. Nogales, M. Gomez, *Lect. Notes Phys.* **2009**, *776*, 61.
- [55] P. Müller-Buschbaum, *Anal. Bioanal. Chem.* **2003**, *376*, 3.

- [56] T. Salditt, T. H. Metzget, J. Peis, B. Reinker, M. Moske, K. Samwer, *Europhys. Lett.* **1995**, 32, 331.
- [57] K. Wang, V. Körstgens, D. Yang, N. Hohn, S. V. Roth, P. Müller-Buschbaum, *J. Mater. Chem. A* **2018**, 6, 4405.
- [58] L. F. Zhang, A. Eisenberg, *Macromolecules* **1999**, 32, 2239.
- [59] H. W. Shen, A. Eisenberg, *J. Phys. Chem. B* **1999**, 103, 9473.
- [60] O. Terreau, L. B. Luo, A. Eisenberg, *Langmuir* **2003**, 19, 5601.
- [61] L. He, S. Pan, J. Peng, *J. Polym. Sci., Part B: Polym. Phys.* **2016**, 54, 544.
- [62] A. F. M. Barton, *Handbook of Solubility Parameters and Other Cohesive Parameters*, CRC Publishers, Boca Raton, FL **1983**, p. 153.
- [63] Y. Li, H. Huang, T. He, *J. Phys. Chem. B* **2010**, 114, 1264.
- [64] W. Zhang, S. Chen, S. Yu, Y. Yin, *J. Cryst. Growth* **2007**, 308, 122.